On modelling viscoelastic flow through abrupt circular 8:1 contractions – matching experimental pressure-drops and vortex structures

H.R.Tamaddon-Jahromi[a], J. E. López-Aguilar[a,b], and M.F. Webster[a†]

[a]*Institute of Non-Newtonian Fluid Mechanics, Swansea University, College of Engineering, Bay Campus, Fabian Way, Swansea, SA1 8EN, UK*
[b]*Facultad de Química, Departamento de Ingeniería Química, Universidad Nacional Autónoma de México (UNAM), Ciudad Universitaria, Coyoacán, CDMX, 04510, Mexico*

Abstract

This study compares and contrasts computational predictions against experimental data for some viscoelastic contraction flows. Nigen and Walters (2002) [1], provides the comparative data-set, the specific flow of interest is an 8:1 abrupt circular contraction, and the constitutive model is that of *swanINNFM(q)* [*swIM*]. Taken against increasing flow-rate, such a model is observed to capture significant vortex-enhancement in these axisymmetric flows, reflecting well the counterpart experimental findings. In addition, rich vortex characteristics are reflected, through evolving patterns of salient-corner, lip-vortex and elastic-corner vortices. A systematic parametric analysis is conducted over three independent and governing material parameters in the model, whilst attempting to interpret rheological adjustment against such changes in flow-structure. Specifically, this has involved variation in solvent-fraction (β), finite-extensibility parameter (L), and extensional-based dissipative parameter (λ_D).

Keywords: Experimental data vs numerical predictions; Boger fluids; flow-structure and pressure-drop; circular contraction flow; lip-, salient- and elastic-corner vortices; *swIM* model

† Correspondence Author: *E-mail address*: m.f.webster@swan.ac.uk

1. Introduction

Amongst other things, this study addresses the problem of matching experimental findings with numerical prediction, covering vortex-structures and experimental-level pressure-drops. That is, as observed in 8:1 circular contraction flows by Nigen and Walters [1]. Close attention is paid to flow-field structure, evolving through flow-rate increase varying material parameters of solvent-fraction (β), finite-extensibility (L), and extensional-based dissipation (λ_D). Each of these material parameters provides an alternative form of rheological response, through extensional viscosity (η_e) and first normal-stress difference (N_1). This permits some insight on the issue of dominant rheological behaviour within this complex flow setting of an 8:1 circular contraction geometry. The solvent-fraction and finite-extensibility parameter significantly adjust both levels of extensional viscosity and first normal-stress difference encountered. In contrast, the extensional-based dissipative parameter, only affects extensional response, and hence provides insight upon separability.

To address the relevant experimental background, Nigen and Walters [1] compared pressure-drops with increasing flow-rates for two sets of Boger fluids of constant shear viscosity, (fluids B1 and B2, polyacrylamide/water–glucose), and for two Newtonian liquids (fluids NS1 and NS2, glucose–water). Axisymmetric and planar contraction configurations were considered for different contraction-ratios (between 2 and 32), including both long- and short-die exit-lengths. Accordingly, a linear relationship was established between pressure-drop and flow-rate. For axisymmetric flows (*not planar counterparts*) and at relatively high flow-rates, differences in pressure-drops between Boger and Newtonian fluids became clearly apparent. These authors also observed that when the die-length was short, such apparent differences were exaggerated over long-length exit-dies. On vortex-structure, the same authors observed vortex-enhancement, with Boger fluids and axisymmetric configurations, a feature absent in planar counterparts. The complex nature and dependency of vortex-enhancement, with its various aspects of vortex-structure (salient-corner vortex, lip-vortex, and elastic-corner vortex behaviour), were found to depend on many factors:- material properties, level of flow-rate, geometry of contraction (planar or axisymmetric), contraction-ratio, shape of contraction (abrupt or rounded), and fluid inertia (see Boger *et al*. [2], Evans and Walters [3], Aboubacar

et al. [4], Rothstein and McKinley [5], Alves *et al.* [6], Oliveira *et al.* [7]). In particular, the importance of the extensional viscosity must be emphasized and the role it plays in the development of vortices (Boger and Walters [8], Boger *et al*. [2]). Furthermore, recent numerical predictions (Tamaddon-Jahromi *et al.* [9, 10], López-Aguilar *et al.* [11, 12]) have confirmed earlier comments by Binding [13], Debbaut and Crochet [14], and Debbaut *et al*. [15] that, high extensional viscosity levels provide large increase in excess pressure-drop (*epd*). An overview of the development of numerical methods and their solutions, when applied to the flow of viscoelastic fluids through planar and axisymmetric contractions, has been described in great detail in Walters and Webster [16], Owens and Phillips [17] and López-Aguilar *et al.* [11, 18]. Such discussion addresses the position for Boger fluids, which manifest constant shear viscosity and strong strain-hardening.

2. Governing equations and flow problem

The relevant equations for the problem at hand are those for incompressible viscoelastic flow, considered under isothermal creeping-flow conditions. This involves field equations for mass conservation, momentum transport and an equation-of-state for stress, represented in non-dimensional form (through scales expressed below) as:

$$\nabla\cdot\mathbf{u}=0, \tag{1}$$

$$\mathrm{Re}\frac{\partial\mathbf{u}}{\partial t}=-\mathrm{Re}\,\mathbf{u}\cdot\nabla\mathbf{u}+\nabla\cdot\boldsymbol{T}-\nabla p, \tag{2}$$

where $\boldsymbol{T}=\boldsymbol{\tau}+2\beta\mathbf{d}$ represents the total-stress, which is itself split into a non-linear polymeric-contribution $\boldsymbol{\tau}$, and a Newtonian solvent-component $\boldsymbol{\tau}_s=2\beta\mathbf{d}$. Here, we adopt the notation where, **u**, **d**, and p represent fluid-velocity, rate-of-deformation tensor $(\nabla\mathbf{u}+\nabla\mathbf{u}^{\dagger})/2$, and hydrodynamic pressure, respectively. The solvent-fraction parameter β is defined as $\beta=\dfrac{\eta_s}{\eta_s+\eta_p}$, which modulates the solvent-to-polymer content in the fluid composition. Then, η_s and η_p are solvent and solute components, respectively, where zero shear-rate viscosity is $\eta_0=\eta_s+\eta_p$.

2.1 The *swanINNFM(q)* (or *swIM*) model

The *swanINNFM(q)* (or *swIM*) model is a hybrid construction based on FENE-CR model (Finite Extendible Nonlinear Elasticity - Chilcott and Rallison, [19]) and White-Metzner models. As such, the relevant theory commences from that of the

FENE-CR model, with the following expression for polymeric-stress ($\boldsymbol{\tau}$), expressed in a conformation-tensor **A**-form as:

$$\mathrm{Wi}\,\overset{\nabla}{\mathbf{A}}+\mathrm{f}(\mathrm{Tr}(\mathbf{A}))(\mathbf{A}-\mathrm{I})=0. \tag{3}$$

The stretch function $\mathrm{f}(\mathrm{Tr}(\mathbf{A}))$ in (3) depends on the extensibility parameter *L*, and is given by:

$$\mathrm{f}(\mathrm{Tr}(\mathbf{A}))=\frac{1}{1-\mathrm{Tr}(\mathbf{A})/L^2}. \tag{4}$$

Then, Kramers rule interrelates polymeric-stress and configuration-tensor, viz.

$$\boldsymbol{\tau}=\frac{(1-\beta)}{\mathrm{Wi}}\mathrm{f}(\mathrm{Tr}(\mathbf{A}))(\mathbf{A}-\mathbf{I}). \tag{5}$$

Above, Reynolds and Weissenberg Group numbers may be defined as: $\mathrm{Re}=\rho \mathrm{U}L_{char}/(\eta_s+\eta_p)$, and $\mathrm{Wi}=\lambda_1\mathrm{U}/L_{char}$, respectively. Accordingly, material parameter are - ρ representing fluid density, (λ_1) a single averaged Maxwellian relaxation time and zero shear-rate viscosity of $\eta_0=\eta_s+\eta_p$. Characteristic scales are taken of U for velocity, and $L_{char}=R_c$ as constriction width for length (thus constructing a characteristic time-scale as L_{char}/U).

The constitutive model used in the present study is that based on the FENE-CR model (as above), taken in combination with an extension-rate dependent viscosity, following the ideology of the White-Metzner model (White and Metzner [20]). The consequence is then the *swanINNFM(q)* model (or *swIM*, in short), (see Tamaddon-Jahromi *et al.* [10], López-Aguilar *et al.* [11, 12], and Garduño *et al.* [21]). The White-Metzner model is derived from network theory of polymers, assuming a flowing polymer of long-chain molecules, connected in a continuously changing network-structure with temporary junctions. As such, White-Metzner viscosity (η) may be taken as a function of rate (second and third) invariants, see Debbaut and Crochet [14], upon which extensional-hardening may be incorporated.

The upshot is a new constitutive equation (*swIM*), which may be expressed on total-stress as:

$$\boldsymbol{T}=\frac{(1-\beta)}{\mathrm{Wi}}\mathrm{f}(\mathrm{Tr}(\mathbf{A}))(\mathbf{A}-\mathbf{I})\phi(\dot{\varepsilon})+2\beta\phi(\dot{\varepsilon})\mathbf{d}, \tag{6}$$

where the dissipative-function $\phi(\dot{\varepsilon})$ is defined as $\phi(\dot{\varepsilon})=1+\left(\lambda_D\dot{\varepsilon}\right)^2$, introducing the extension-rate $(\dot{\varepsilon})$, with its invariant dependence, and a dissipative extensional material time-scale parameter of $\left(\lambda_D\right)$, see Tamaddon-Jahromi *et al.* [10] for further

detail. This completes the White-Metzner viscosity (η) component, via the dissipative-function $\phi(\dot{\varepsilon})$.

2.2 Material properties with *swIM*

The associated rheometrical functions for the *swIM* model can be represented as:

$$\eta = 1,$$
$$N_1^{shear} = \frac{2(1-\beta)\mathrm{Wi}\dot{\gamma}^2}{\mathrm{f}}, \tag{7}$$
$$\eta_e = 3\phi(\dot{\varepsilon})\beta + 3\phi(\dot{\varepsilon})(1-\beta)\left[\frac{\mathrm{f}^2}{\mathrm{f}^2 - \mathrm{f}\,\mathrm{Wi}\dot{\varepsilon} - 2\mathrm{Wi}^2\dot{\varepsilon}^2}\right].$$

Hence below, we compare and contrast the particular characteristics, and variation under parameter adjustment, of the two important quantities of extensional viscosity (η_e) and first normal-stress difference (N_1). Essentially, to furnish rheological explanation for the various flow phenomena observed in the complex flow scenarios under investigation.

Solvent fraction adjustment: (1/9≤ β <0.9)*:* Figure 1a,b provides the associated material functions for *swIM*[λ_D=0.075, L=5] with variation in solvent-fraction, 1/9≤ β ≤0.9. Enhancement in η_e is clearly apparent within *swIM*(l_D≠0) properties, when compared to those for FENE-CR (*swIM*(l_D=0)). Larger values of solvent-fraction (β) correspond to dilute or less-entangled systems (larger solvent composition); whilst lower β-values correspond to highly-entangled systems (larger solute/polymeric composition). As such, larger values of stretch and stress are anticipated under greater polymeric content. The *swIM* model predicts a constant shear viscosity, whilst inheriting from FENE-CR, a first normal-stress difference that is weaker than the strong Oldroyd-B quadratic-form. Particularly, one notes the *distinct increase in level of* η_e *as the solvent-fraction (β) decreases*. This is in evidence at $\lambda_1\dot{\gamma}$>5 units, where there is almost a 6-times increase in η_e from β=0.9 to β=1/9. In contrast, there is monotonic decline apparent in N_1 with increasing solvent-fraction. Here, and at the rate of $\lambda_1\dot{\gamma}$=3 units, N_1 declines from O(10) units at β=1/9, to O(1) units at β=0.9.

Comparably under the same solvent-fraction adjustment, but at the slightly higher rate of $\lambda_1\dot{\gamma}$ =5 units, N_1-values drop from O(20) to O(3) units.

Extensibility parameter adjustment: (5≤ L <10) The counterpart characterisation for *swIM*[λ_D=0.075, β=0.9] with elevation of extensibility parameter (L), 5≤ L <10, is displayed in Figure 1c,d. Response with *swIM* for large-L asymptotes towards Oldroyd-B behaviour in both N_1 and η_e. In particular, at low strain-rate (≤0.5 units), extensional viscosity response practically mirrors that of Oldroyd-B. Subsequently, and up to strain-rates of O(4) units, *swIM*-η_e follows FENE-CR response; yet thereafter, showing significant departure between *swIM*-η_e and FENE-CR-η_e.

When comparing decreasing-β against rising-L, with its impact on extensional viscosity (η_e), Figure 1a,c, one may note the following: η_e sharply rises at $\lambda_1\dot{\gamma}$ =5*10^{-1} units under (L-increase), whilst equivalently, it rises somewhat earlier at $\lambda_1\dot{\gamma}$ =10^{-1} units with (β-decrease). In addition, the level of η_e for L=5 (β=1/9) is almost two-times larger than for L=10 (β=0.9). From past experience, this would lead one to anticipate larger vortex growth/enhancement with *β-decrease* than with *L-increase*.

The counterparts of first normal-stress difference response (N_1) and shear-viscosity (η, constant) of *swIM* replicate FENE-CR properties. Furthermore, considering weakening-characteristics of N_1 at larger rates (as in Figure 1d with L-decrease), against that of (Figure 1b with β-increase), upon close inspection one can gather, that *decreasing-L conveys even greater N_1-weakening than does β-increase*.

Dissipative-parameter adjustment: (0.0≤ λ_D <1.0)*:* Figure 2 provides the corresponding {η_e, N_1} material functions for *swIM*[L=5, β=0.9] with λ_D–variation, 0≤λ_D≤1.0. Here, a rising trend in extensional viscosity is clearly observed for *swIM*(λ_D>0), when compared to that for base-form, FENE-CR(λ_D=0). Yet, this is considerably less than Oldroyd-B response for strain-rates $\lambda_1\dot{\varepsilon}$ ≥0.5 units. Notably, the (λ_D=0.1)-curve captures FENE-CR(λ_D=0) base-form up to its second limiting-plateau at high rates; it departs in response around strain-rates $\lambda_1\dot{\varepsilon}$ ~O(3) units; then, rising sharply thereafter. Relative to subsequent elevation to (λ_D=0.4), this departure point

occurs somewhat earlier at $\lambda_1\dot{\varepsilon}$ ~0.9 units, thereby bypassing the characteristic plateau of FENE-CR(λ_D=0). Equivalently for λ_D=1.0, such departure has shifted by over a decade earlier to $\lambda_1\dot{\varepsilon}$ ~0.3 units. Once again, first normal-stress difference response (N_1) and shear-viscosity (η) of *swIM* follow from FENE-CR, being independent of λ_D. Therefore, under (λ_D-adjustment), *only extensional viscosity can be responsible for vortex-growth characteristics* (as here, there is no impact on N_1). This lies in distinct contrast to the counterpart position under {L, β}-adjustment.

3. Algorithm and problem specification

Figure 3a (domain) and Figure 4 (pressure-drop) illustrate the background detail to the flow problem at hand, that of the 8:1 circular abrupt contraction flow. This information indicates the target experimental data of Nigen and Walters [1] for the predictive solutions to replicate. Here, the pressure-drop (ΔP) and flow-rate (Q) are scaled, respectively, using base-values extracted from [1] of ΔP_0=10^5 Pa and $\mathrm{Q}_0 = \mathrm{Q}_0\left[\dfrac{1\mathrm{g/s}}{0.0014\,\mathrm{g/mm^3}}\right]$, taking the fluid density as ρ ~ 1.4 mg/mm^3.

One may derive a relationship between the alternative definitions used in the literature for Weissenberg number in experiments and computations, viz, experimentally $(Wi_{\lambda_1}^{Exp} = \lambda_1^{Exp}\dfrac{Q}{\pi R_c^3},\ \ \lambda_1^{Exp} = 0.16s)$, and computationally $(Wi_{\lambda_1}^{Sim} = \lambda_1^{Sim}\dfrac{Q}{\pi R_c^3} = \lambda_1^{Sim}\bar{U}/L_{char})$. The principal reason for such differences lies in the choice made, in each case, between the particular factor within the Weissenberg number to hold fixed. Experimentally, it is often more convenient to work with a single fluid (fixing λ_1^{Exp}) and to vary flow-rate; whilst computationally, it is often more convenient to work at a fixed flow-rate (retaining fixed boundary conditions) and to vary the material relaxation time (λ_1^{Sim}). Nevertheless, one may establish a scaling factor between $Wi_{\lambda_1}^{Exp}$ and $Wi_{\lambda_1}^{Sim}$, in order to compare experimental and simulation findings on a one-to-one basis. In this particular instance, this provides an equivalent and relational scaling factor of 6.25, so that $Wi_{\lambda_1}^{Sim} = 6.25Wi_{\lambda_1}^{Exp}$; see [10, 11] for a more detailed explanation. Note, in this study, findings are conveyed in terms of

a relative flow-rate (Q/Q_0) measure, based on [1], whilst selecting $R_c = L_{char} = 0.2237$ and $\lambda_1^{Sim} = 1$, whereby $Q / Q_0 = 0.0352\, Wi_{\lambda_1}^{Sim}$.

The principal finite-element meshing used to represent this geometric configuration, of Figure 3a (medium mesh), reflects 1707 quadratic-elements and 3634 nodes, with 22768 degrees-of-freedom (*dof*) . Mesh refinement has been employed over three levels of gradation *h*={coarse, medium, refined}, from which consistency upholds the medium mesh on solution precision. Overall, triangular element mesh structure is illustrated, in Figure 3a. There, the various mesh characteristics are quantified, with details recorded of total numbers of elements, nodes, and degrees of freedom. One notes that differences in solutions through mesh refinement (medium and refined meshes), with *swIM*[L=5, λ_D=0.075, β=0.9] model, are found to be less than 0.2% in first normal stress difference (N_1), along the centreline of the flow away from boundary layer influence, see Figure 3b. Hence, justifying the choice of the medium refined-mesh upon which to base the subsequent study.

Creeping flow conditions are assumed, so that ($\mathrm{Re} \approx O(10^{-2})$), wherein momentum convection considerations are negligible. To maintain compatibility with the composition of the Boger fluids used in the experiments, the *base-setting* for solvent-fraction is taken as β=0.9. Subsequently, variation and departure in solvent-content is addressed, within this detailed parameter sensitivity analysis. Likewise, yet in contrast, variation is considered under extensibility-parameter (L), and dissipative extensional material time-scale parameter (λ_D).

The numerical method presented in this article is based on a hybrid finite-element and a finite-volume algorithm, which follows a three-stage time-splitting semi-implicit formulation. This scheme combines a finite-element (*fe*) discretisation (Taylor-Petrov-Galerkin/incremental Pressure-Correction) for the conservation-momentum equation set, with a cell-vertex finite-volume (*fv*) scheme for the differential constitutive equation. The details of this algorithm have been extensively documented elsewhere (see, for example, Wapperom and Webster [22]; Belblidia *et al.* [23]; Webster *et al.* [24, 25]; López-Aguilar *et al.* [11, 18]). New and novel aspects to the computational procedures include - imposing velocity-gradient boundary conditions at the flow centreline (*VGR*-correction); a discrete correction for continuity; absolute-representation for the constitutive-model structure-function

(*ABS-f*); and adopting continuation through steady-state solutions whilst increasing flow-rate (see López-Aguilar *et al.* [11]). The first three of these additional strategies have been found to considerably enhance robustness in extraction of steady-state solutions. Flow-rate continuation is also an important consideration, when concerned with direct comparison between experimental results and numerical predictions.

4. Discussion on Computational Predictions

4.1 Numerical predictions versus experimental measurement – *base-case scenario*

On pressure-drop: Figure 4 displays the charting of scaled experimental pressure-drop data from Nigen and Walters [1], against present numerical predictions. In this, the dissipative extensional-viscous time-scales chosen are λ_D ={0.05, 0.075, 0.1}. Henceforth, for clarity in notation, Q/Q_0 is referred to as scaled (Q). Accordingly with all three values of λ_D, one can observe that *swIM*–solutions well-capture the experimental data, whilst covering the *low* flow-rate regime of $Q\leq 1$. Shifting towards higher flow-rates, one notes that the *pressure-drop*(λ_D=0.05)-solution *underestimates* the experimental position, whilst the *pressure-drop*(λ_D=0.1)-solution provides *overestimation*. Then consistently, the intermediate *pressure-drop*(λ_D=0.075)-solution provides a superior match to the experimental target data. Note in addition, that present Newtonian predictions agree well with Syrup 2-fluid pressure-drop data, extracted up to $Q\sim 1.5$; subsequently, slightly underestimating experimental readings (with larger experimental error bars being anticipated at these higher rates).

On vortex-activity: In addition for mid-range value (λ_D=0.075)-solutions, Figure 5 displays a canvas of three distinct phases of vortex build-up, a central feature to this analysis. This information identifies the construction of salient-corner vortices (*scv*); the emergence of lip-vortices (*lv*); their coalescence; and lastly, the establishment of elastic-corner-vortices (*ecv*). Such a position is strongly supported by the experimental evidence reported in Nigen and Walters [1].

As such, inspecting the detail in Figure 5, salient-corner vortices are observed with Q-increase up to Q=0.09 units, of vortex intensity (vortex strength) $|\psi_{min}| = 0.0064$ units. Then, a lip-vortex *first appears* around Q=0.12 units, proving weaker in strength at this juncture than its salient-corner counterpart. Subsequently, the lip-

vortex grows in strength to Q=0.15 units ($|\psi_{min}|$=0.0103 units), whereupon it has almost doubled the rotational intensity of the salient-corner vortex. Furthermore, one discerns nearly one order of magnitude increase in *lv*-intensity, between these two flow-stations from Q=0.12 to Q=0.15 units. At and around the flow-rate of Q=0.2 units, transition is captured, just prior to the engulfing of the weaker salient-corner vortex with the stronger lip-vortex. Beyond Q=0.2 units and with subsequent flow-rate increase, these vortex patterns evolve into a substantial elastic-corner vortex, displaying features of an ever-growing reattachment-length on the upstream-wall, and a gradual switch in curvature of the vortex separation-line. This may be observed in the vortex-structures represented between Q=0.35 and Q=1.6 units, that reveal this switch between concave-shape to convex-shape.

Clearly, advancing steady-state solutions through an incremental continuation-protocol and flow-rate (Q)-increase, as opposed to fluid-elasticity (λ_1)-increase, has the tendency to generate considerably more exaggerated vortex-activity (see Tamaddon-Jahromi *et al.* [10], López-Aguilar *et al.* [11, 12]). For example, see Figure 5 for evidence on this matter, where vortex-intensity at Q=1.9 units ($|\psi_{min}|$ =9.166 units) is almost two orders of magnitude larger than at Q=0.25 units ($|\psi_{min}|$ = 0.0992 units).

4.2 Parametric Variation: *solvent-fraction (β), extensibility parameter (L), dissipative parameter (λ_D)*

In the present study, specific focus is placed upon the flow response under the influence of variation over these three rheometric factors: solvent-fraction (β), finite-extensibility parameter (L), and the extensional-based dissipative parameter (λ_D). In such a complex contraction-flow setting, varying the solvent-fraction (β) and finite-extensibility parameter (L), significantly adjusts the pertaining levels of extensional viscosity (η_e) and first normal-stress differences (N_1). Recall in addition, by increasing the extensional-based dissipative parameter (λ_D), one is able to discern the precise role that extensional viscosity (alone) has, upon associated solution-response (with no change in N_1-properties in pure-shear).

Influence of solvent fraction adjustment: (1/9≤ β <0.9)

The overall impact of solvent-fraction (β) adjustment on vortex-structure and intensity is presented in Figures 6-9. Such data covers solutions for fixed, yet ever rising flow-rates, with successive ramping between [Q=0.035, Q=0.09] (low), to [Q=0.12, Q=0.2] (medium), and finally, Q=1.6 units (high).

At the *lowest flow-rate* (Q=0.035, Figure 6a), only salient-corner vortex (*scv*) activity is detected; so being devoid of any lip-vortex (*lv*) activity. Vortex-size and intensity vary considerably with solvent-fraction reduction, from (β=0.9, highly-dilute, $|\psi_{min}|$=0.0008) to (β=1/9, highly-polymeric, $|\psi_{min}|$=0.0020), substantiating a *2.5*-times boost in vortex-intensity.

With the second *flow-rate* reported (Q=0.09, Figure 6b), the *first evidence* for lip-vortex formation is detected (*lv*, $|\psi_{min}|$=0.0047) as one transcends the various solvent-fraction ratios to (β=0.7), see also Figure 9a. This is accompanied by salient-corner vortex presence (*scv*, $|\psi_{min}|$=0.0064). At slightly lower solvent-fractions of (β=0.6), such lip-vortex activity considerably strengthens (*lv*, $|\psi_{min}|$=0.0102), to even supersede the salient-corner vortex-intensity (*scv*, $|\psi_{min}|$=0.0087). Upon decreasing solvent-fraction somewhat further, from (β=0.6) to (β=0.5), the lip-vortex *subsumes* the salient-corner vortex, to emerge as a *single strong* elastic-corner vortex (*ecv*). These features are accompanied by the appearance of a convex-shaped vortex separation-line (see Figure 6b). One notes in passing that, *ecv*-intensity doubles from (β=0.5, $|\psi_{min}|$=0.0164) to (β=0.3, $|\psi_{min}|$=0.0307); and then subsequently, tripling to (β=1/9, $|\psi_{min}|$=0.0446). Previously, such vortex features have been observed experimentally by Boger *et al.* [2, 26], when switching between alternative composition Boger fluids of solvent-fractions (β=0.87) and (β=0.73). In that work, the circular contractions covered geometric aspect ratios 2:1, 4:1 and 16:1.

Next in Figure 7, one considers ramping of flow-rate to the more elevated levels of Q=0.12 and Q=0.2 units (medium Q-phase). Here, conspicuously at (Q=0.12, Figure 7a), lip-vortex formation now appears earlier in β-decline, and hence, for more dilute systems at (β=0.9), see also Figure 9a. Subsequent trends are similar to the foregoing, noting that now, lip-vortex growth consumes and dominates *scv*-activity at the more-dilute solvent-fraction of (β=0.7), whilst leading to the elastic-corner vortex-structure.

With concentration increase from (β=0.7 down to β=1/9), there is almost an 80% increase in *ecv*-intensity. During this phase, the more prominent shape-switch is beginning to appear in the elastic-corner vortex separation-line, from convex-to-concave; this gradually becomes more prominent with decline in β-setting.

Still larger *ecv*-intensities are realised upon yet further increase in flow-rate, through stages Q={0.2, 0.56, 1.6} units (see Figures 7b, 8, 9, and Table 1; high Q-phase). Table 1 also conveys the fringe behaviour of (*scv/lv*)-appearance and the pattern of how this occurs at *ever decreasing flow-rate as solvent-fraction declines*. Overall, one may gather that *decline in solvent-fraction* clearly *stimulates considerable elevation in vortex-size*, and this in turn, *impacts on pressure-drop*. So, for example, at a flow-rate Q=0.56 units, *ecv*-intensity (β=1/9, $|\psi_{min}|$=6.795 units) is almost *8-times* that for (β=0.9, $|\psi_{min}|$=0.8853 units). One notes that, maxima in *ecv*-intensity ($|\psi_{min}|$=16.377 units) is captured with a solvent-fraction of (β=0.6) and a flow-rate of Q=1.6 units (beyond which stable steady-state solution become intractable).

On Q-increase at fixed solvent-fraction: From an alternative stance, one may also consider the position at *fixed solvent-fraction* and flow-rate increase. Then, for dilute-systems at (β=0.9), with some 20% increase in flow-rate, from Q=0.12 to Q=0.15 units, *lv*-intensity increases by nearly 85%; whilst comparably, *scv*-intensity increases by almost 40%. In contrast, for more concentrated systems at (β=1/9) and with the same increase in flow-rate, *ecv*-intensity rises by nearly 55%, see Figures 7a and 10a. At (β=0.9) in Figure 9a, one may also detect erratic behaviour in *scv*-growth with flow-rate rise (Q=0.09 to Q=0.15, medium rate-range), just prior to *ecv*-onset. Note also that, in this same figure, *scv*-decline at the intermediate flow-rate of Q=0.12 (β=0.9) is accompanied with a lip-vortex.

On vortex-activity and N_1: Furthermore, one may extract a degree of correlation between vortex-activity and first normal-stress difference N_1, considering the solvent-fraction range, $1/9 \leq \beta \leq 0.9$, for (Q=0.15 units) in Figure 10a. From this data, it is apparent that the various vortex-structures (*scv*, *lv*, and *ecv*) correlate closely with the corner-patterns in N_1-fields. One may gather from this evidence that elasticity, through first normal-stress difference, strongly influences the formation of such vortex-structures (as observed in López-Aguilar *et al.* [12]). Furthermore in Figure

10b, various N_1-profiles are presented for $1/9 \leq \beta \leq 0.9$; at (r=0) along the centreline (a pure-extension line); and at (r=1) along the downstream-wall (a pure-shear line) and upstream through the domain. When considering the centerline profile, there is almost six-fold increase in N_1-maximum between β=0.9 (N_1_max=12 units) to β=1/9 (N_1_max=70 units). This realization correlates well with the extensional viscosity plot for *swIM* of Figure 1a, where equivalently there is some six-fold increase in η_e when $\lambda_1\dot{\gamma} > 5$. Moreover under solvent-fraction adjustment, along the downstream-wall (r=1) in shear, the N_1-peak (183 units, β=1/9) near the contraction-zone is almost twelve times larger than its equivalent, N_1-peak (15 units, β=0.9).

Influence of finite extensibility adjustment: (5≤ L <10)

With rising flow-rate (Q), Figure 11 conveys the influence on vortex-structure/intensity of (L–rise). There are no significant changes to observe in *scv*-intensities at relatively low-levels of flow-rate with increasing L (refer back to β-decrease). Here, *scv*-intensity remains practically constant (~O($5*10^{-3}$) units), over the range $5 \leq L \leq 10$, for Q=0.035 (not shown) up to Q=0.12 units (Figure 11b); also the separation-line remains concave in shape. In contrast, and over the same range of flow-rates, such vortex intensity is almost two-orders of magnitude larger with β-adjustment (see Figures 6, 7a); indicating the relative importance between these two factors.

Furthermore, at Q=0.12 units, a *lip-vortex* appears when {L=5, β=0.9}, Figures 11b, 12. With L–rise, from L=6 to L=10, this feature then merges into the *salient-corner* (*not elastic-corner*) vortex; residing firmly within the salient-corner neighbourhood whilst tapering down to the re-entrant corner. This is a *distinct and new feature to the low-rate scenario, occurring under L–rise and high solvent-fraction*. Such an observation is somewhat different to findings above, when decreasing solvent-fraction at Q=0.12 units (Figure 7a). To distinguish, under β-drop, *lip-vortex* activity evolves into an *elastic-corner vortex*; being then accompanied by adjustment in outer-shape of the vortex separation-line from concave-to-convex. These differences at Q=0.12 units may be associated with the *earlier rate-rise in extensional viscosity* under β-change, as opposed to L-parameter change. Note that, whilst solvent-fraction drops from β=0.9 to β=1/9, extensional viscosity levels

increase from ~O(7) to ~O(40) units. Alternatively, with *L*-rise from *L*=5 to *L*=10, η_e increases from ~O(7) to ~O(20) units; thus, barely half as much. Hence, *one may attribute counterpart extensional viscosity response to these observed trends in vortex-growth*. This feature becomes even more stark at yet larger flow-rates. For instance, consider the relative positions at flow-rate *Q*=0.56 units – there, *β*-decrease {from 0.9 to 1/9} has a much stronger influence on vortex-growth, when compared to *L*-increase {from *L*=5 to 10}. This can be gathered from solutions at the extremities: viz {*L*=5, *β*=1/9} vortex-intensity is almost three-times larger than for {*L*=10, *β*=0.9}. Moreover, interpreting from respective extensional viscosity plots (lower η_e with *L*-change in comparison to *β*-change), one may expect to gather more exaggerated solution response at larger rates with *β*-drop compared to *L*-rise (see Figure 8 versus Figure 11d; and Figure 9b versus Figure 12).

Influence of **dissipative-parameter** ***adjustment: (0.0≤ λ_D <1.0)***

With rising flow-rate (*Q*), Figure 13 conveys the counterpart story to that above, at three selected flow-rates (*Q*=0.09, *Q*=0.12, and *Q*=0.15), now considering the influence of (λ_D)–variation on vortex-structure. Here, solvent-fraction is set at (*β*=0.9) and extensibility parameter is (*L*=5). One notes that vanishing-λ_D implies collapse of *swIM* extensional-viscosity enhancement, then recovering to base-form FENE-CR. Larger λ_D–factors correspond to extensional viscosity elevation when $\lambda_1\dot{\varepsilon}$>0.5 (see Figure 2a). At *Q*=0.09 units and with rise in λ_D to λ_D~0.3, there is little significant change to note in *scv*-intensity. This may be associated with a delayed rise in η_e up to $\lambda_1\dot{\gamma}$=1, which agrees with observations above under *L*-increase (small vortex-intensities at low-rates with delayed rise in η_e). However, as flow-rate rises, it is clearly apparent that increase in λ_D stimulates considerable adjustment in vortex-structure. One may observe such impact at *Q*=0.09 units, in switching between parameters {λ_D=0.0 to λ_D=0.8} (see Figure 13a and Figure 14a, 0<*Q*≤0.15). Under this *Q*-setting, each feature of *salient-corner vortex*, *lip-vortex* and *elastic-corner vortex* has been observed; as indicated in Figures 13, 14. Interestingly, one may detect the first signs of *lip-vortex appearance*, by monitoring reduction in *scv*-intensity, between λ_D=0.1 to λ_D=0.2 solutions (Figure 13a). For example at *Q*=0.09 units, no

lip-vortex appears with *L-increase* (β=0.9, λ_D=0.075), whilst a *lip-vortex* is first detected with *β-decrease* at β=0.7 (L=5, λ_D=0.075). Once more, this concurs with the various levels of η_e observed under {λ_D, *L*, β}-adjustment. Again, at (*Q*=0.09 units), a *lip-vortex* first appears in advance of λ_D at λ_D=0.3; this then significantly magnifies, by nearly an order-of-magnitude at λ_D=0.6. Such a trend is also accompanied with strong adjustment in intensity of the *salient-corner vortex*. Moreover, and with still further elevation of dissipative-parameter to λ_D=0.7, as earlier, the *lip-vortex* evolves into an *elastic-corner vortex* (displaying a concave/convex-shaped separation-line).

Furthermore, and upon increasing flow-rate to *Q*=0.12 units (Figure 13b, Figure 14a, 0<*Q*≤0.15), such a *lip-vortex* appears earlier in λ_D-adjustment; even at (λ_D=0.0). So, at (λ_D=0.0), *lv*-intensity is around twenty–fold that at (λ_D=0.4). This is the largest *lip-vortex* observed with {λ_D, *L*, β}-adjustment. In addition, considering instead *elastic-corner vortex* appearance, this also appears earlier at λ_D=0.5 for *Q*=0.12 units; whilst in contrast and for still lower flow-rates of *Q*=0.09, such an *elastic-corner vortex* is more delayed and appears at λ_D=0.8. This goes hand-in-hand with the sharp increase noted in (η_e), for $\lambda_D \geq 0.5$.

Furthermore, with a higher level of flow-rate of *Q*=0.15 units and at λ_D=0.1, the *lv*-intensity is nearly one order of magnitude larger than at the lower flow-rate of *Q*=0.12 units (Figure 13b, Figure 14a, 0<*Q*≤0.15). Beyond λ_D=0.2 and with increasing λ_D, the lip-vortex evolves into an elastic-corner vortex (see Figure 13c).

From this position onwards, and with subsequent flow-rate rise, through stages *Q*={0.2, 25, 0.56, 1.05 1.6} units, a large *ecv*-intensity dominates. That is, with increasing λ_D–parameter, from (λ_D=0) to (λ_D=0.5) (see vortex-intensity plot, Figure 14b, 0.15<*Q*≤1.6)). For instance, at flow-rate *Q*=0.2 units, *ecv*-intensity (λ_D=0.5) is almost *twice* that for (λ_D=0.0). Moreover, amongst {λ_D, *L*, β}-adjustment, the largest *ecv*-intensity ($|\psi_{min}|$=18.053 units) has been recorded at *Q*=1.6 units, and that corresponds to λ_D = 0.3, Figure 14b.

So, overall with $\{\beta\ ,\ L,\ \lambda_D\}$-adjustment, major differences are detected in the medium rate-range with *Q*-rise. There, β-decrease shows significant differences in vortex- structure (convex-shaped vortex separation-line, larger vortex intensities and *ecv*-intensity); that is in comparison to *L*-increase (still concave-shaped) and λ_D-increase (concave-to-convex shaped). Yet, λ_D-increase characteristics follow more closely to trends under β-decrease, than to *L*-increase; indicating again, the strong influence of (η_e) on vortex characteristics.

5. Conclusions

This work stands as a benchmark study on circular contraction flows, for Boger fluids covering a range of different rheological parameters - as in, solvent-fraction (β), finite-extensibility (L), and extensional-based dissipation (λ_D). The influence of extensional viscosity (η_e) and first normal-stress difference (N_1) on flow structure has been examined and demonstrated, through predictions with the *swIM* model, under constant shear viscosity characteristics.

Advancing steady-state solutions through an incremental continuation-protocol and flow-rate (*Q*)-increase, as opposed to the fluid-elasticity (λ_1)-increase, has the tendency to generate considerably more exaggerated vortex activity. From this investigation, findings have revealed that different flow-structures in *salient-corner* (*scv*), *lip-* (*lv*) and *elastic-corner vortices* (*ecv*), have each been successively observed. Hence, confirming the experimental findings of Nigen and Walters [1]. Here, with β-adjustment, *first evidence* of *lip-vortex*-formation is observed for *Q*=0.09 units at the solvent-fraction (β=0.7), whilst the *latest evidence* of *lip-vortex*-formation is detected at β=0.9 for *Q*=0.15 units. In addition, at relatively low *Q*-levels (*Q*=0.12), vortex-intensity is almost two-orders of magnitude larger with β-adjustment than with increasing *L*.

More generally, differences in vortex-growth characteristics and enhancement with $\{\beta, L, \lambda_D\}$ adjustment may be associated with earlier rate-rise and level in extensional viscosity under β-change, as opposed to *L*- and λ_D-changes. Here, for meaningful

comparisons in (η_e) across parameters, one must take care to adjust a single parameter at a time, and to balance others whilst doing so. Furthermore, one may detect the first signs of *lip-vortex appearance*, by monitoring reduction in *scv*-intensity, when anticipating vortex-growth with increasing flow-rate. Moreover, it is shown that the various vortex-structures generated (*scv*, *lv*, and *ecv*) correlate closely with corner-patterns in N_1-fields. One may gather from this evidence that elasticity, through *localised* first normal-stress difference, is responsible for the formation of such vortex-structures. Yet, in addition, one can infer from vortex-trends observed under λ_D-increase (with characteristics of only η_e-increase, no N_1-change), that η_e-strengthening also strongly impacts on vortex-growth and structures formed.

The common trend observed in vortex-growth with flow-rate rise is to form a salient-corner vortex *at low-rates*, which gives way to coexistence with lip-vortex formation in a *low-to-mid rate range*, prior to coalescence. Under $\{\beta,\ \lambda_D\}$-change, the lip-vortex has been observed to dominate in this coalescence (convex-concave separation-line), in leading towards a strong elastic-corner vortex at *larger flow-rates* (with a concave separation-line). Alternatively, under *L*-rise, the coalescence emerges with salient-corner vortex characteristics. The eye of this vortex subsequently strengthens and gradually shifts towards the re-entrant corner through the *low-to-mid rate range*, mimicking a lip-vortex. Finally, at *larger flow-rates*, once again a strong elastic-corner vortex is recovered. The subtle balance in rheology, and most particularly in η_e, is primarily held responsible for these noted differences.

Additionally, a secondary aim of this study has been realised, in establishing agreement between the experimental pressure-drop data of Nigen and Walters [1] for 8:1 contraction-flows, and *swIM* computational predictions. In itself, this work stands as a major step forward, advancing beyond our earlier studies on contraction-expansion flows, where both rounded-corner and abrupt-corner configurations were presented (Tamaddon-Jahromi *et al.* [10], López-Aguilar *et al.* [11, 12]). Accordingly, one may observe that suitably large pressure-drops can be attained with appropriate selection of extensional time-scale λ_D. If anything, this study has tied down such excess pressure-drop generation, alongside its counterpart vortex activity.

Acknowledgment

This work was presented by H.R Tamaddon-Jahromi at the Spring Symposia INNFM Lake Vyrnwy April 2017. The authors are grateful to the helpful advice from Professor Ken Walters throughout the course of this work. Financial support from PAIP (5000-9172, FQ UNAM, Mexico), PAPIIT (IA105818, UNAM, Mexico), Consejo Nacional de Ciencia y Tecnología (CONACYT, Mexico) and support from the Zienkiewicz Centre for Computational Engineering, College of Engineering, Swansea University, UK, are gratefully acknowledged.

References

[1] S. Nigen, K. Walters, Viscoelastic contraction flows: comparison of axisymmetric and planar configurations, J. Non-Newton Fluid Mech. 102 (2002) 343-359.

[2] D.V. Boger, D.U Hur, R.J Binnington, Further observations of elastic effects in tubular entry flows, J. Non-Newton Fluid Mech. 20 (1986) 31-49.

[3] R.E. Evans, K. Walters, Flow characteristics associated with abrupt changes in geometry in the case of highly elastic liquids, J. Non-Newton Fluid Mech. 20 (1986) 11-29.

[4] M. Aboubacar, H. Matallah, H.R. Tamaddon-Jahromi, M.F. Webster, Numerical prediction of extensional flows in contraction geometries: hybrid finite volume/element method, J. Non-Newton Fluid Mech. 104 (2002) 125-164.

[5], J.P. Rothstein, G.H. McKinley, The axisymmetric contraction-expansion: the role of extensional rheology on vortex growth dynamics and the enhanced pressure drop, J. Non-Newton Fluid Mech. 98 (2001) 33-63.

[6] M.A. Alves, P.J. Oliveira, F.T. Pinho, On the effect of contraction ratio in viscoelastic flow through abrupt contractions, J. Non-Newton Fluid Mech. 122 (2004) 117-130.

[7] Mónica S.N. Oliveira, Paulo J. Oliveira, Fernando T. Pinho, Manuel A. Alves, Effect of contraction ratio upon viscoelastic flow in contractions: The axisymmetric case, J. Non-Newton Fluid Mech. 147 (2007) 92–108.

[8] D.V. Boger, K. Walters, *Rheological Phenomena in Focus*, Elsevier Science Publishers B.V. (1993).

[9] H.R. Tamaddon-Jahromi, M.F. Webster, P.R. Williams, Excess pressure drop and drag calculations for strain-hardening fluids with mild shear-thinning: Contraction and falling sphere problems, J. Non-Newton Fluid Mech. 166 (2011) 939–950.

[10] H.R.Tamaddon-Jahromi, I.E.Garduño, J.E. López-Aguilar, M.F Webster, Predicting Excess pressure drop (*epd*) for Boger fluids in expansion-contraction flow, J. Non-Newton Fluid Mech. 230 (2016) 43–67.

[11] J.E. López-Aguilar, M.F. Webster, H.R. Tamaddon-Jahromi, K. Walters, Numerical vs experimental pressure drops for Boger fluids in sharp-corner contraction flow, Physics of Fluids 28 (2016) 103104.

[12] J.E. López-Aguilar, M.F. Webster, H.R. Tamaddon-Jahromi, M. Pérez-Camacho, O. Manero, Contraction-ratio variation and prediction of large experimental pressure-drops in sharp-corner circular contraction-expansions - Boger fluids, J. Non-Newton Fluid Mech. 237 (2016) 39-53.

[13] D.M. Binding, Further considerations of axisymmetric contraction flows. J. Non-Newton Fluid Mech. 41 (1991) 27-42.

[14] B. Debbaut, M.J. Crochet, Extensional effects in complex flows, J. Non-Newton Fluid Mech. 30 (1988) 169-184.

[15] B. Debbaut, M.J. Crochet, H.A. Barnes, K. Walters, Extensional effects in inelastic liquids, Xth Inter. Congress on Rheology, Sydney (1988) 291-293.

[16] K. Walters, M.F. Webster, The distinctive CFD challenges of computational rheology, Inter. J. for Numer. Meth. in Fluids 43 (2003) 577-596.

[17] R.G. Owens, T.N. Phillips, *Computational Rheology*, Imperial College Press, London, (2002).

[18] J.E. López-Aguilar, M.F. Webster, H.R. Tamaddon-Jahromi, O. Manero, High-Weissenberg predictions for micellar fluids in contraction–expansion flows, J. Non-Newton Fluid Mech. 222 (2015) 190–208.

[19] M.D. Chilcott, J.M. Rallison, Creeping flow of dilute polymer solutions past cylinders and spheres, J. Non-Newton Fluid Mech. 29 (1988) 381-432.

[20] J.L. White, A.B. Metzner, Development of constitutive equations for polymeric melts and solutions, J. Appl. Polym. Sci. 7 (1963) 1867-1889.

[21] I.E Garduño, H.R. Tamaddon-Jahromi, M.F. Webster, The falling sphere problem and capturing enhanced drag with Boger fluids, J. Non-Newton Fluid Mech. 231 (2016) 26–48.

[22] P. Wapperom, M.F. Webster, A second-order hybrid finite-element/volume method for viscoelastic flows, J. Non-Newton Fluid Mech.79 (1998) 405-431.

[23] F. Belblidia, H. Matallah, M.F Webster, Alternative subcell discretisations for viscoelastic flow: Velocity-gradient approximation. J Non-Newt Fluid Mech. 151 (2008) 69-88.

[24] M.F. Webster, H.R. Tamaddon-Jahromi, M. Aboubacar, Transient Viscoelastic Flows in Planar Contractions, J Non-Newt Fluid Mech. 118 (2004) 83-101.

[25] M.F. Webster, H.R. Tamaddon-Jahromi, M. Aboubacar, Time-Dependent Algorithms for Viscoelastic Flow: Finite Element/Volume Schemes, Numer. Meth. Par. Diff. Equ. 21 (2005) 272-296.

[26] D.V. Boger, Viscoelastic flows through contractions, Ann. Rev. Fluid Mech. 19 (1987) 157-82.

Figure captions

Table 1. Salient-corner (*scv*), lip-vortex (*lv*) and elastic corner (*ecv*) appearance, $0<Q/Q_0\leq 1.6$ units, *swIM*[L=5, λ_D=0.075], various β

Figure 1. a, c) Extensional viscosity, b, d) first normal-stress difference for Oldroyd-B and *swIM* models, λ_D=[0.0, 0.075], a, b) $1/9\leq\beta\leq 0.9$, L=5; c, d) $5\leq L\leq 10$, β=0.9

Figure 2. a) Extensional viscosity b) first normal-stress difference for Oldroyd-B and *swIM* models, λ_D=[0.0-1.0], β=0.9, L=5

Figure 3. a) Zoomed mesh sections, 8:1 contraction geometry (Coarse: *elements=868, nodes=1897, dof=11897*; Medium: *elements=1707, nodes=3634, dof=22768;* Refined: *elements=2762, nodes=5787, dof=36235*); b) N_1 at centerline (coarse, medium, refined solutions), Q=0.15 units; *swIM*[L=5, λ_D=0.075, β=0.9]

Figure 4. Pressure-drop vs flow-rate, Nigen and Walters, [1] 8:1 *axisymmetric* contraction, experimental data vs *swIM*(λ_D =0.05, 0.075, 0.1; L=5, β=0.9) predictions

Figure 5. Streamlines, $0.035\leq Q/Q_0\leq 1.9$; *swIM*[β=0.9, L=5, λ_D=0.075]

Figure 6. Streamlines, a) Q/Q_0=0.035, b) Q/Q_0=0.09; *swIM*[L=5, λ_D=0.075]; $1/9\leq\beta\leq 0.9$

Figure 7. Streamlines, a) Q/Q_0=0.12, b) Q/Q_0=0.2; *swIM*[L=5, λ_D=0.075]; $1/9\leq\beta\leq 0.9$

Figure 8. Streamlines, a) Q/Q_0=0.56, b) Q/Q_0=1.6; *swIM*[L=5, λ_D=0.075]; $1/9\leq\beta\leq 0.9$

Figure 9. a) Salient-corner (*scv*) and lip-vortex (*lv*)elastic corner b) elastic-corner (*ecv*) vortex intensity (ψ_{min}), $0<Q/Q_0\leq 1.6$; *swIM*[L=5, λ_D=0.075]; $1/9\leq\beta\leq 0.9$

Figure 10 a) Streamlines ψ, first normal-stress difference N_1-fields; b) first normal-stress difference N_1-profiles at r=0 (symmetry line) and r=1; Q/Q_0=0.15; *swIM*[L=5, λ_D=0.075]; $1/9\leq\beta\leq 0.9$

Figure 11. Streamlines, a) Q/Q_0=0.09, b) Q/Q_0=0.12, .15, c) Q/Q_0=0.2, .25, d) Q/Q_0=0.56, 1.6; *swIM*[[β=0.9, λ_D=0.075], $5\leq L\leq 10$

Figure 12. Vortex intensity (ψ_{min}), $0<Q/Q_0\leq 1.6$; *swIM*[[β=0.9, λ_D=0.075], $5\leq L\leq 10$

Figure 13. Streamlines, a) Q/Q_0=0.12, b) Q/Q_0=0.12, c) 0.15; *swIM*[β=0.9, L=5], various λ_D

Figure 14. a) Salient, lip, and b) elastic-corner vortex intensity (ψ_{min}); *swIM*[β=0.9, L=5], $0<Q/Q_0\leq 1.6$, various λ_D

Table 1. Salient-corner (*scv*), lip-vortex (*lv*) and elastic corner (*ecv*) appearance, $0<Q/Q_0\leq 1.6$ units; *swIM*[L=5, λ_D=0.075], various β

$\downarrow Q/Q_0$	β								
	0.9	**0.8**	**0.7**	**0.6**	**0.5**	**0.4**	**0.3**	**0.2**	**1/9**
0.035	***scv***	***scv***	***scv***	***scv***	***scv***	***scv***	***scv***	***scv***	***scv***
0.09	***scv***	***scv***	***scv/lv***	***scv/lv***	*ecv*	*ecv*	*ecv*	*ecv*	*ecv*
0.12	***scv/lv***	***scv/lv***	*ecv*	*ecv*	*ecv*	*ecv*	*ecv*	*ecv*	*ecv*
0.15	***scv/lv***	*ecv*	*ecv*	*ecv*	*ecv*	*ecv*	*ecv*	*ecv*	*ecv*
0.2, 0.56	*ecv*	*ecv*	*ecv*	*ecv*	*ecv*	*ecv*	*ecv*	*ecv*	*ecv*
1.6	*ecv*	*ecv*	*ecv*	*ecv*	-	-	-	-	-

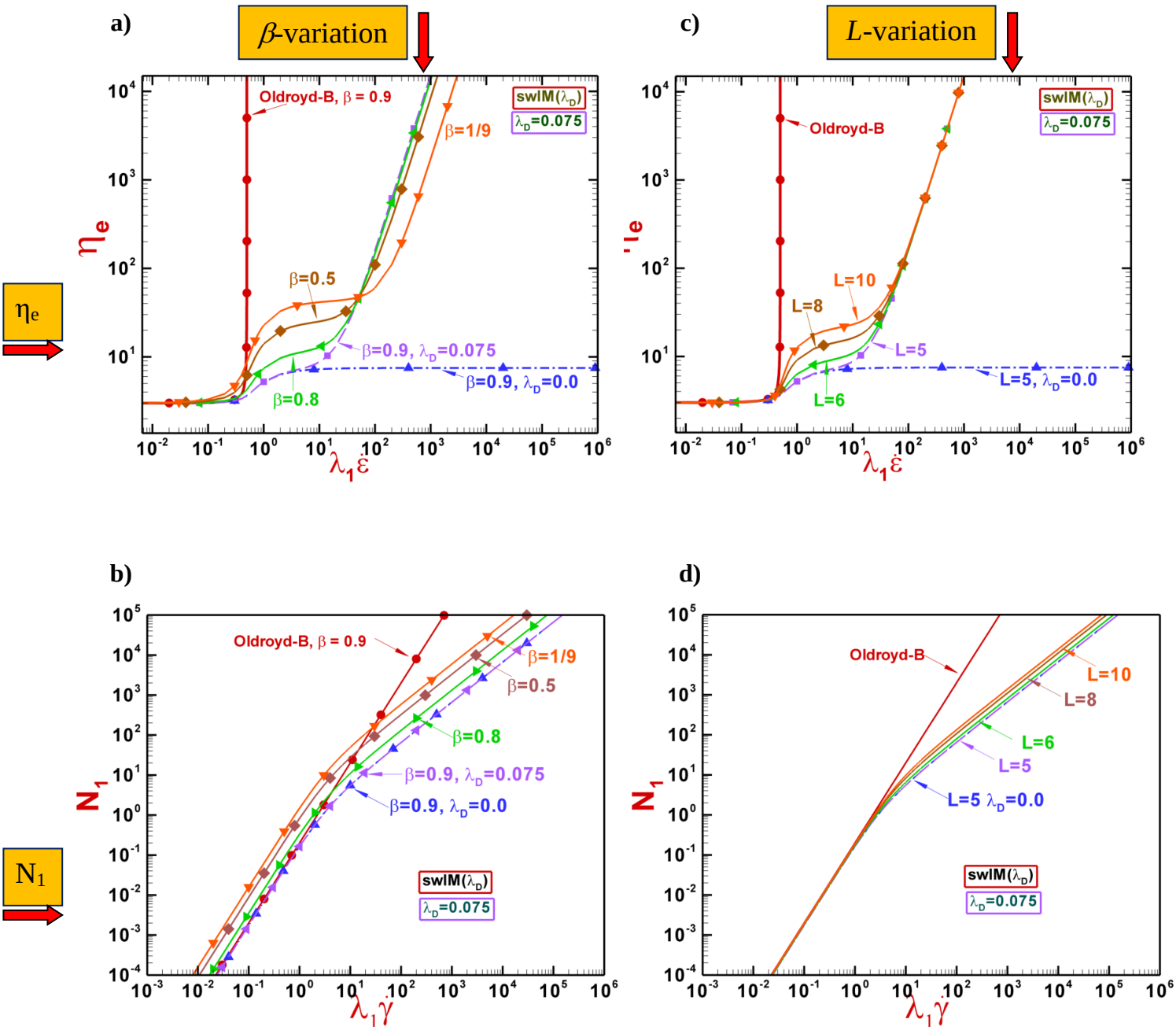

Figure 1. a), c) Extensional viscosity; b), d) first normal-stress difference; Oldroyd-B and *swIM* models; λ_D=[0.0, 0.075], a),b) 1/9≤ β ≤0.9, L=5; c), d) 5≤ L ≤10, β=0.9

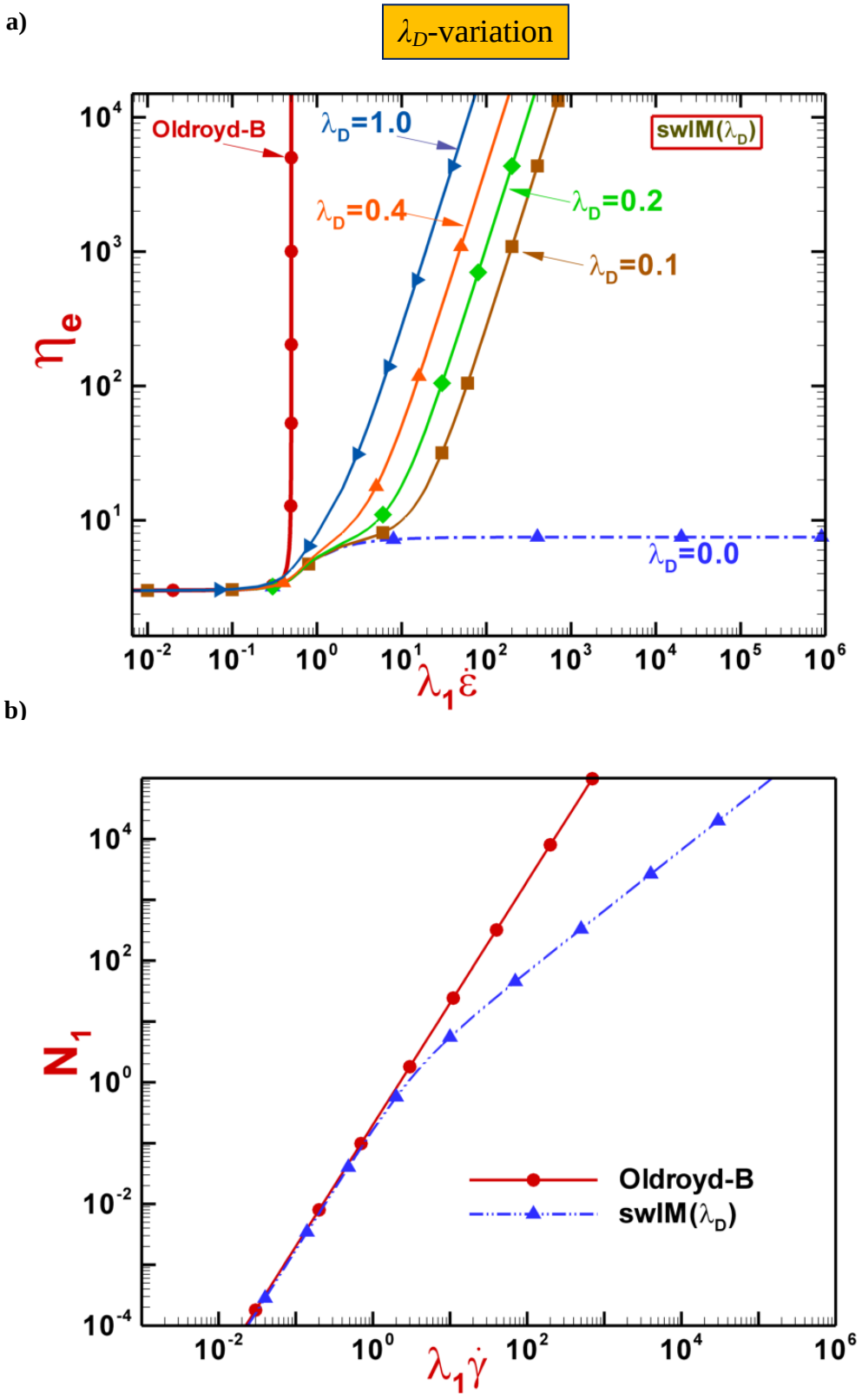

Figure 2. a) Extensional viscosity b) first normal-stress difference for Oldroyd-B and *swIM* models, λ_D=[0.0-1.0], β=0.9, L=5

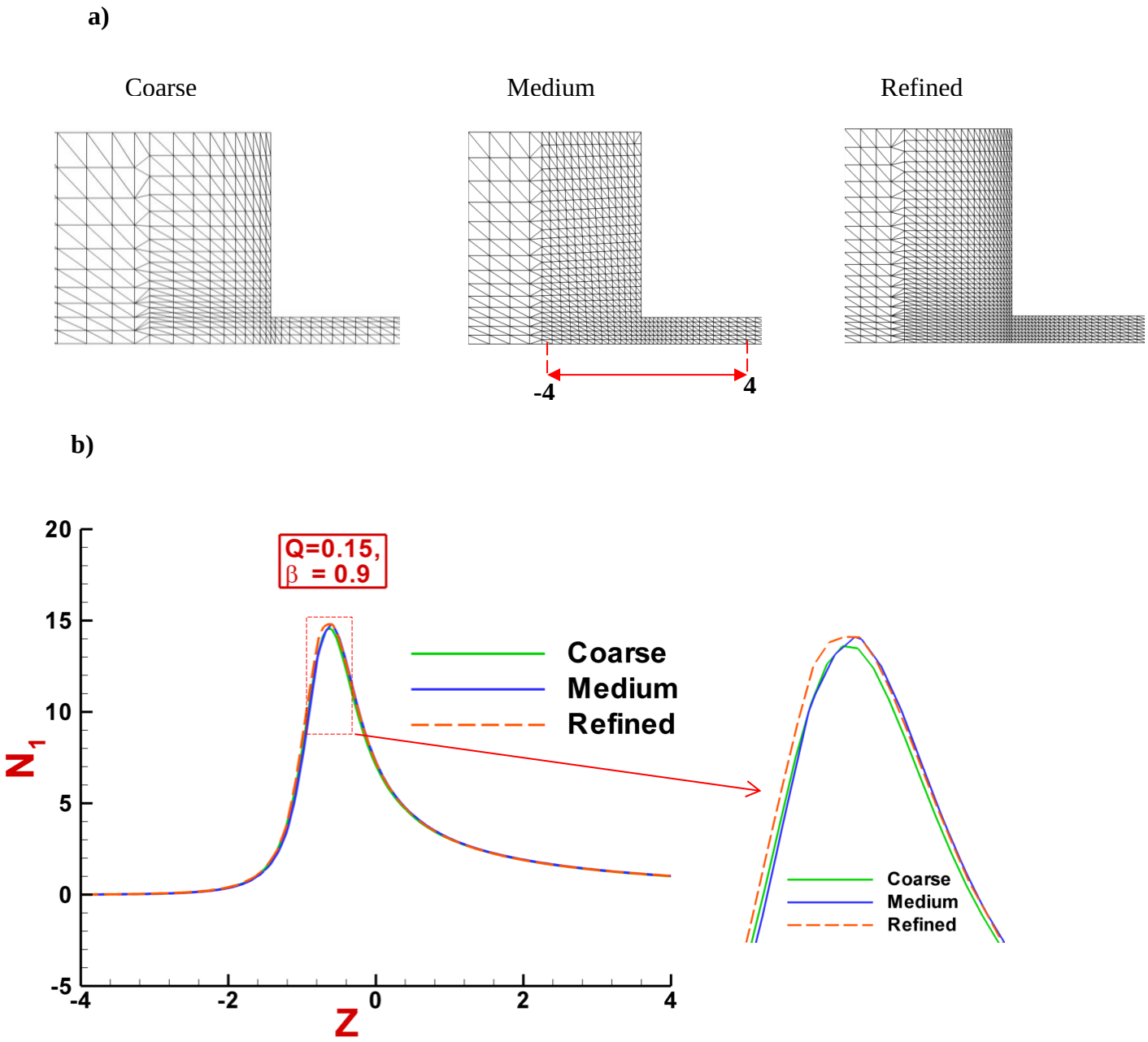

Figure 3 a) Contraction mesh sections, 8:1 contraction (Coarse: *elements=868, nodes=1897, dof=11897*; Medium: *elements=1707, nodes=3634, dof=22768;* Refined: *elements=2762, nodes=5787, dof=36235*);
b) N_1 at centerline (coarse, medium, refined solutions), Q=0.15 units; *swIM*[L=5, λ_D=0.075, β=0.9]

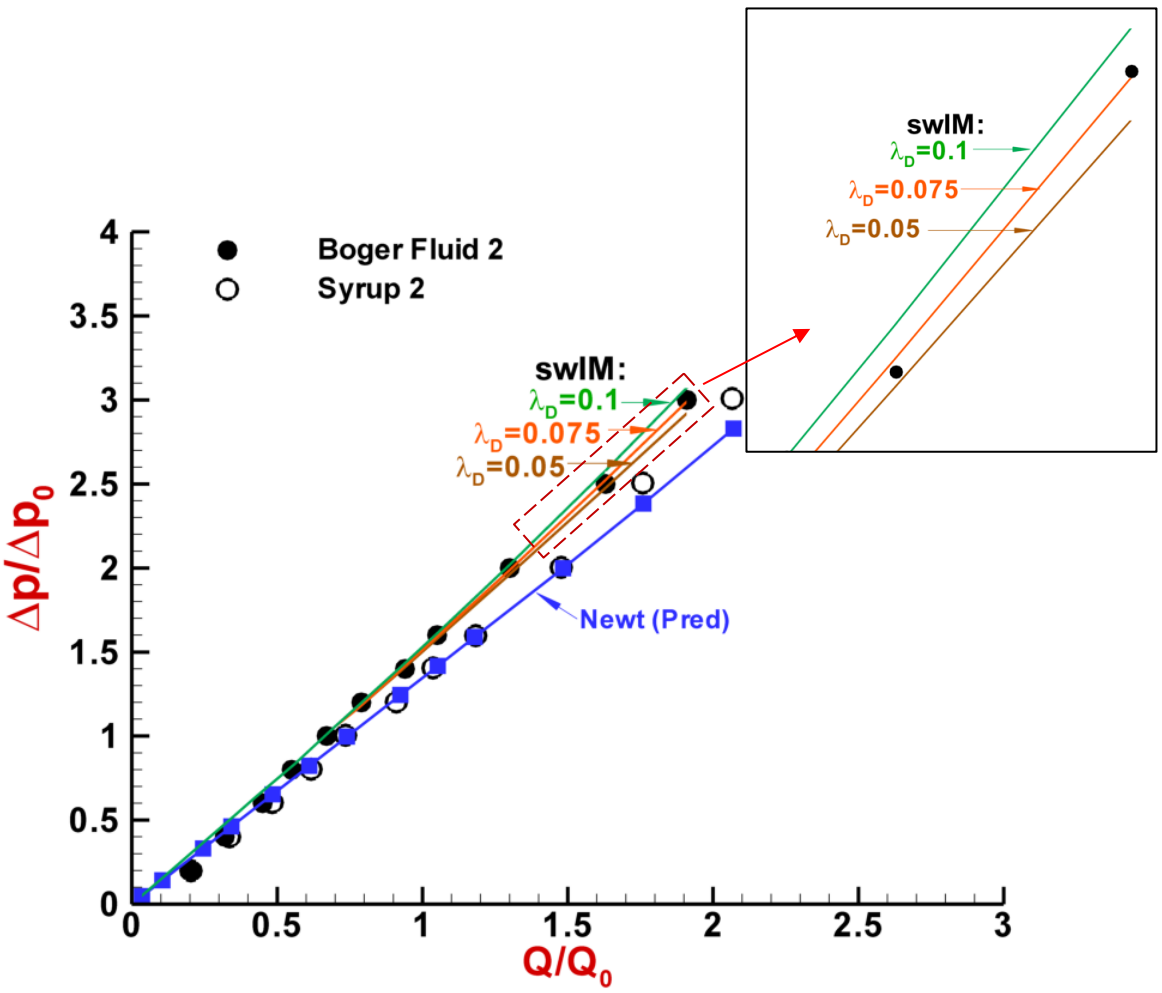

Figure 4. Pressure-drop vs flow-rate, Nigen and Walters [1], 8:1 *axisymmetric* contraction, experimental data vs *swIM[*(λ_D =0.05, 0.075, 0.1; L=5, β=0.9)] predictions

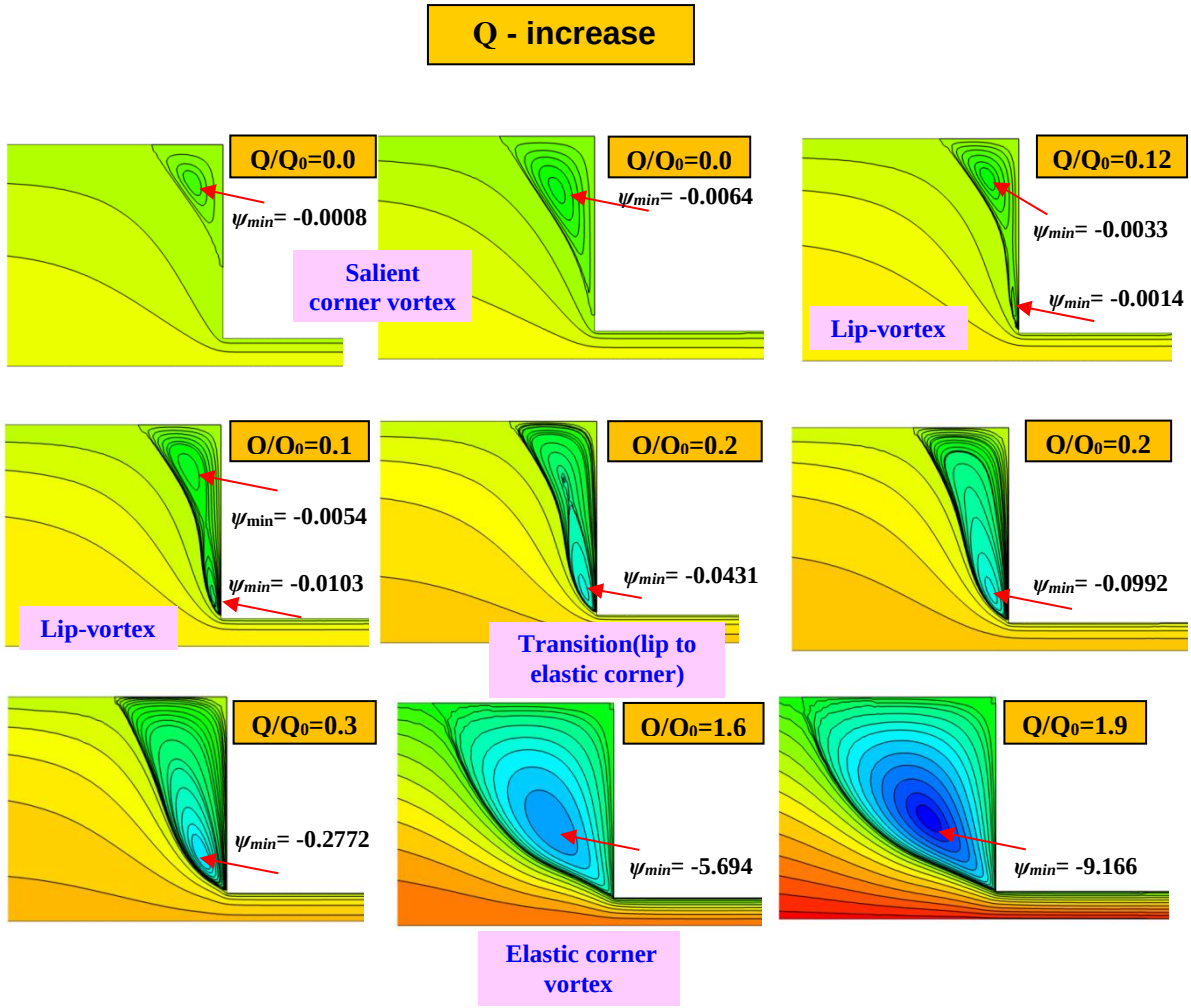

Figure 5. Streamlines, $0.035 \leq Q/Q_0 \leq 1.9$; *swIM*[$\beta$=0.9, L=5, λ_D=0.075]

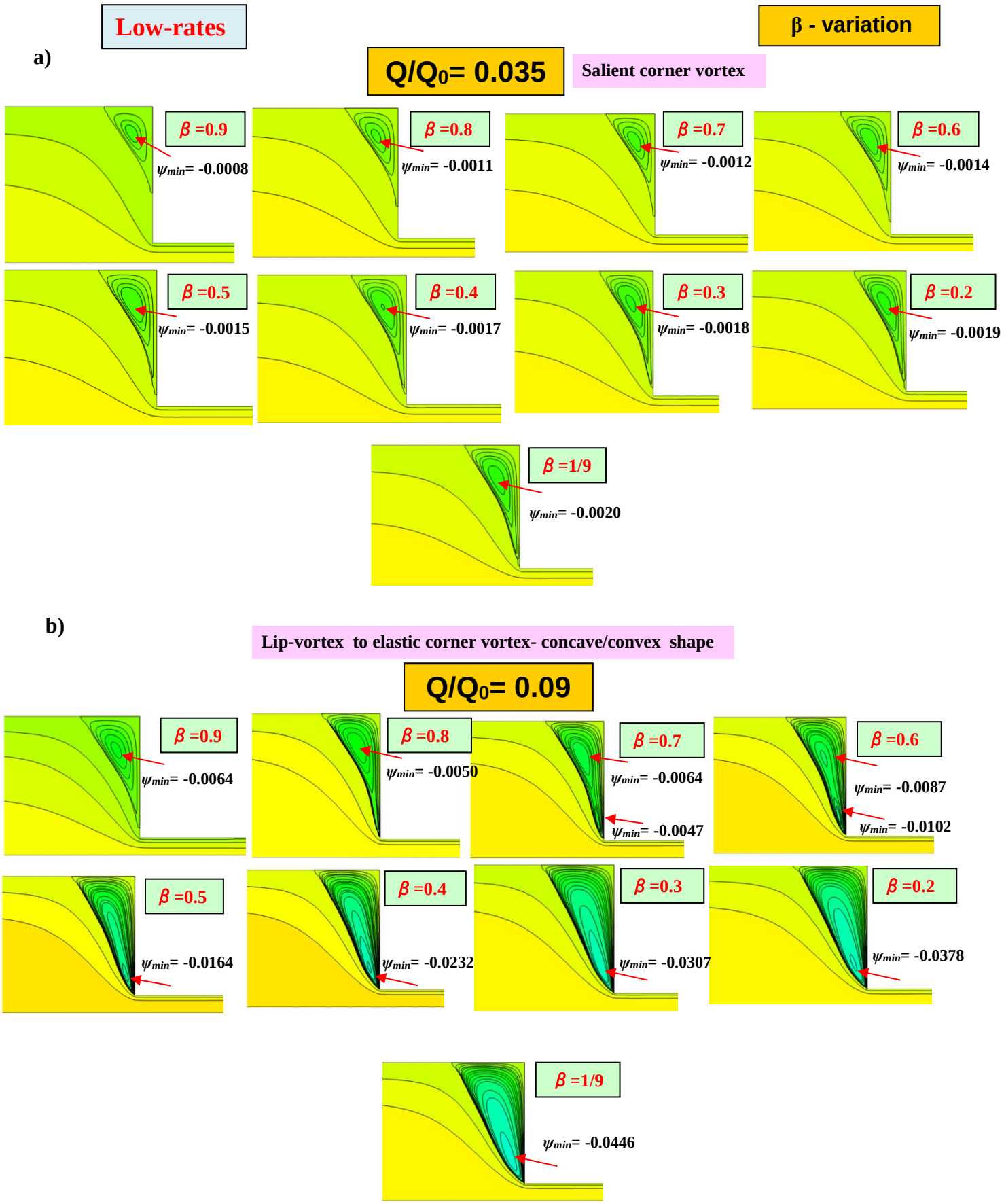

Figure 6. Streamlines, a) Q/Q_0=0.035, b) Q/Q_0=0.09; *swIM*[L=5, λ_D=0.075]; 1/9≤β≤0.9

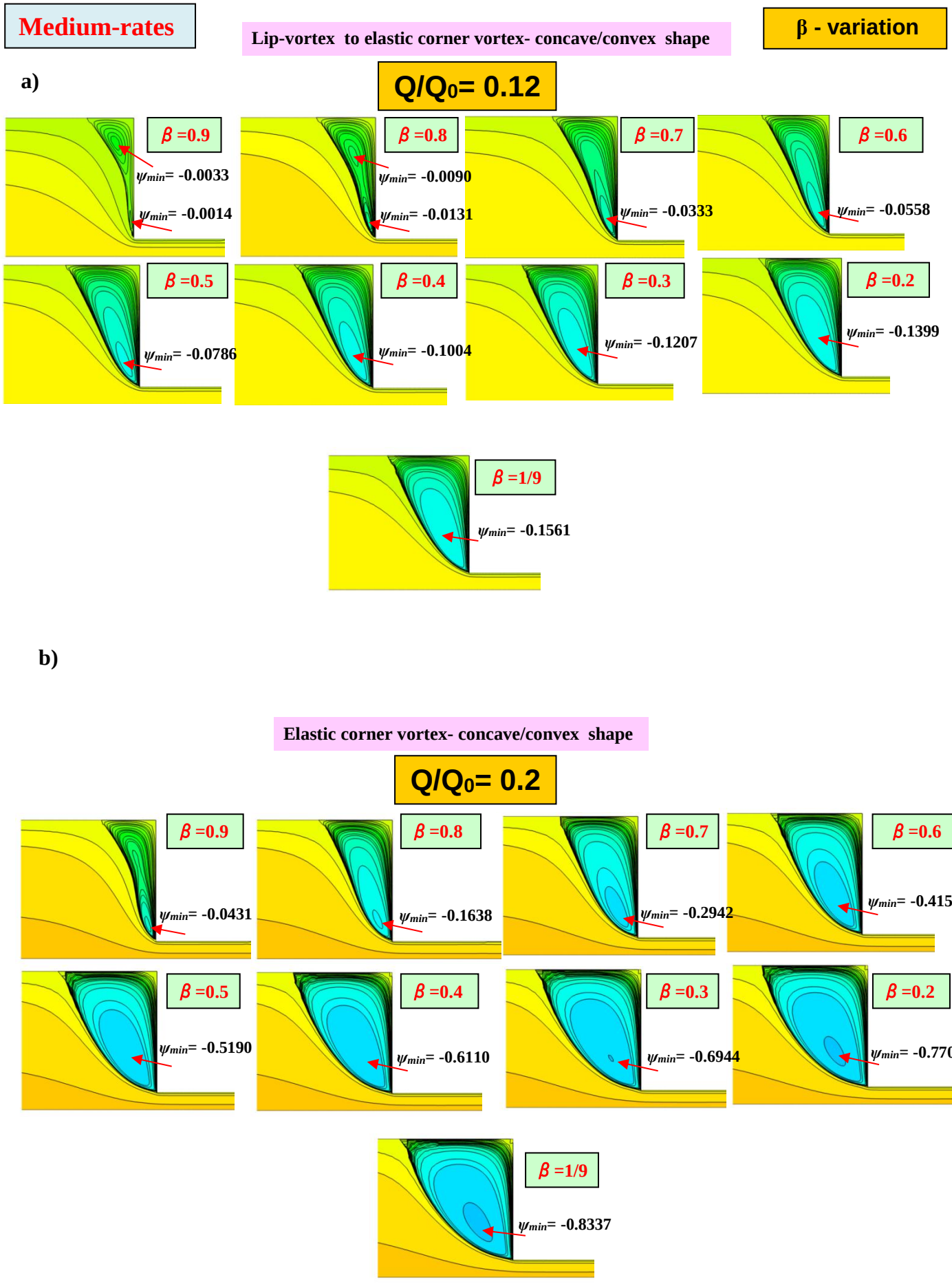

Figure 7. Streamlines, a) Q=0.12, b) Q/Q_0=0.2; *swIM*[L=5, λ_D=0.075]; 1/9≤β≤0.9

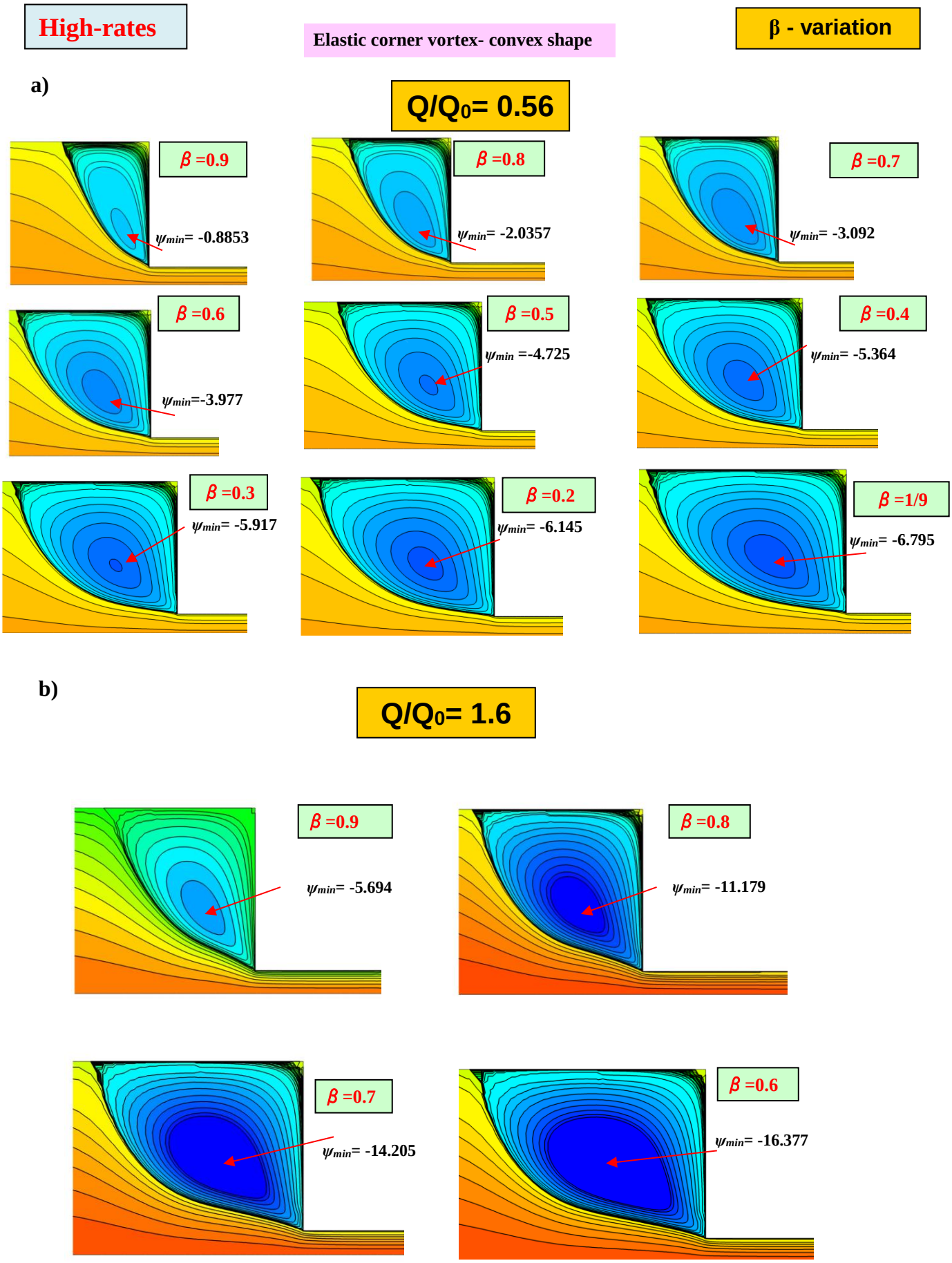

Figure 8. Streamlines, a) Q/Q_0=0.56, b) Q/Q_0=1.6; *swIM*[L=5, λ_D=0.075]; $1/9 \leq \beta \leq 0$

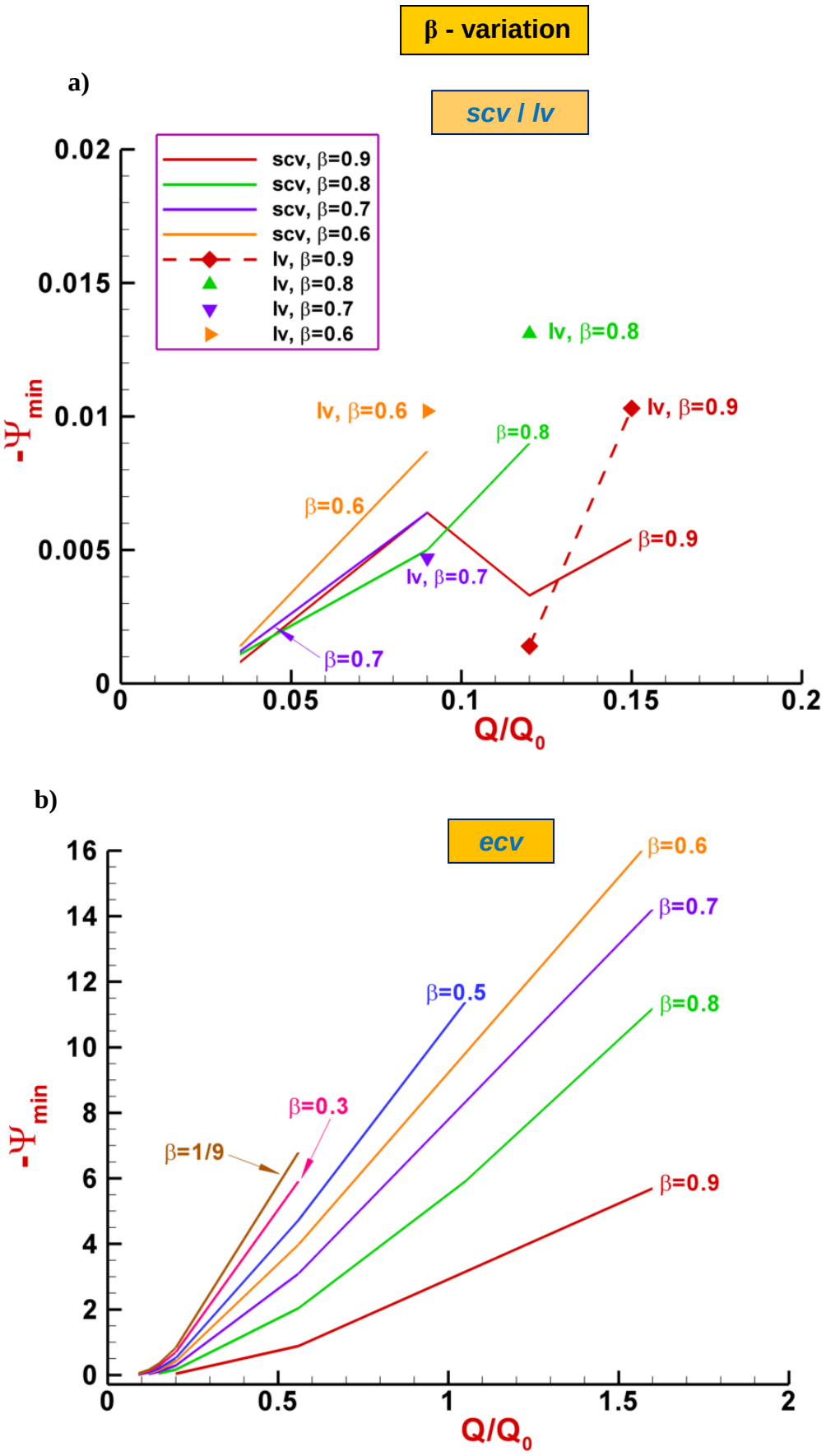

Figure 9. a) Salient (*scv*), lip (*lv*) and b) elastic-corner (*ecv*) vortex intensity (ψ_{min}), $0<Q/Q_0\leq 1.6$; *swIM*[L=5, λ_D=0.075]; $1/9\leq\beta\leq 0.9$

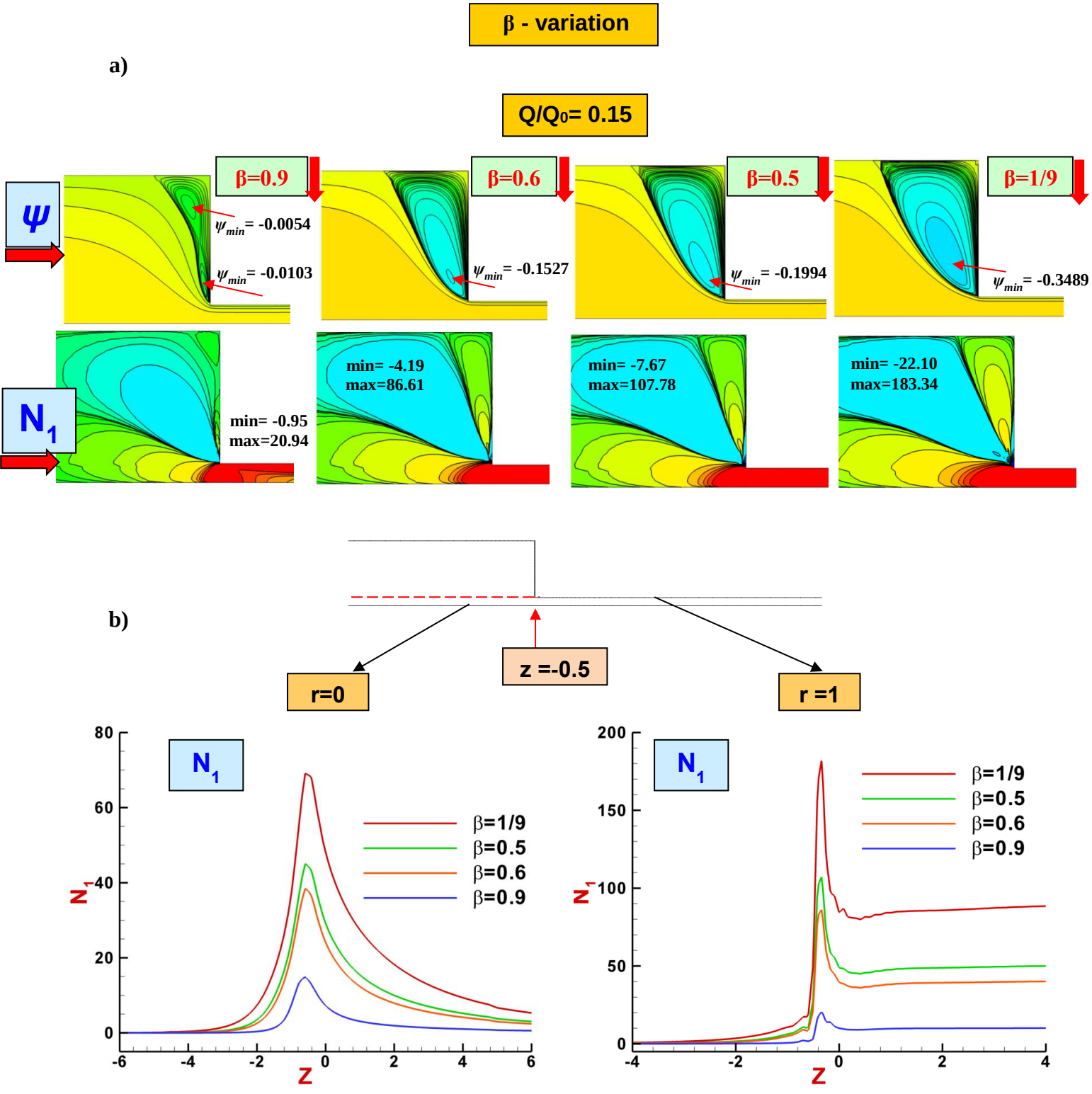

Figure 10 a) Streamlines ψ, first normal-stress difference N_1-fields; b) first normal-stress difference N_1-profiles at r=0 (symmetry line) and r=1; Q/Q_0=0.15; *swIM*[L=5, λ_D=0.075]; 1/9≤β≤0.9

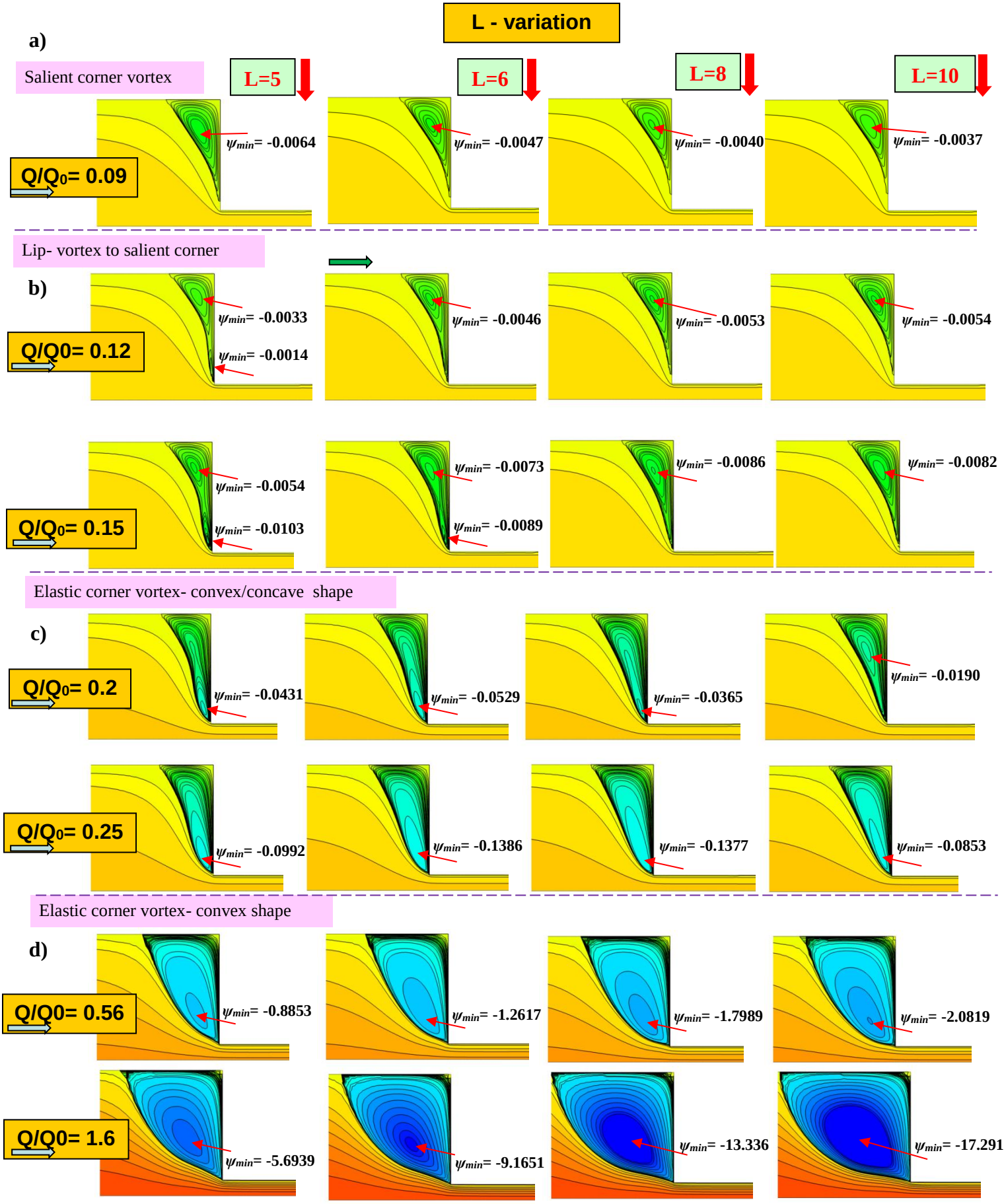

Figure 11. Streamlines, a) Q/Q_0=0.09, b) Q/Q_0=0.12, .15, c) Q/Q_0=0.2, .25, d) Q/Q_0=0.56, 1.6; *swIM*[[β=0.9, λ_D=0.075], 5≤L≤10

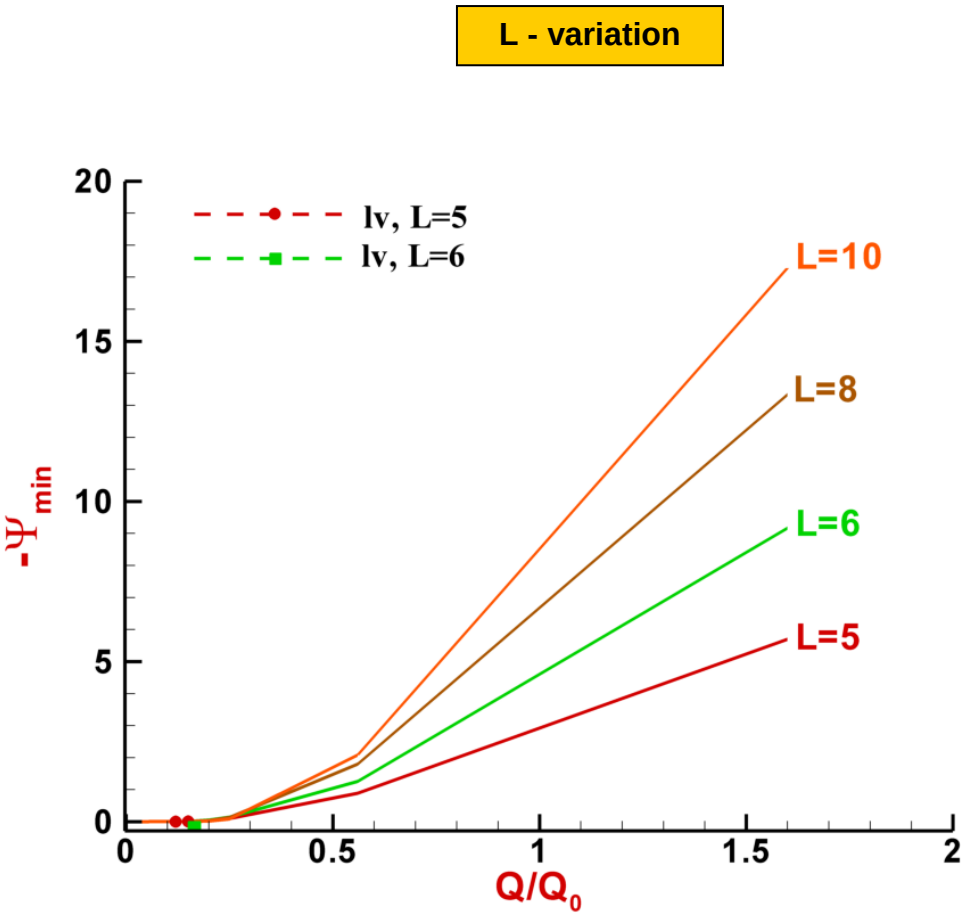

Figure 12. Vortex intensity (ψ_{min}), $0<Q/Q_0\leq 1.6$; *swIM*[[β=0.9, λ_D=0.075], $5\leq L\leq 10$

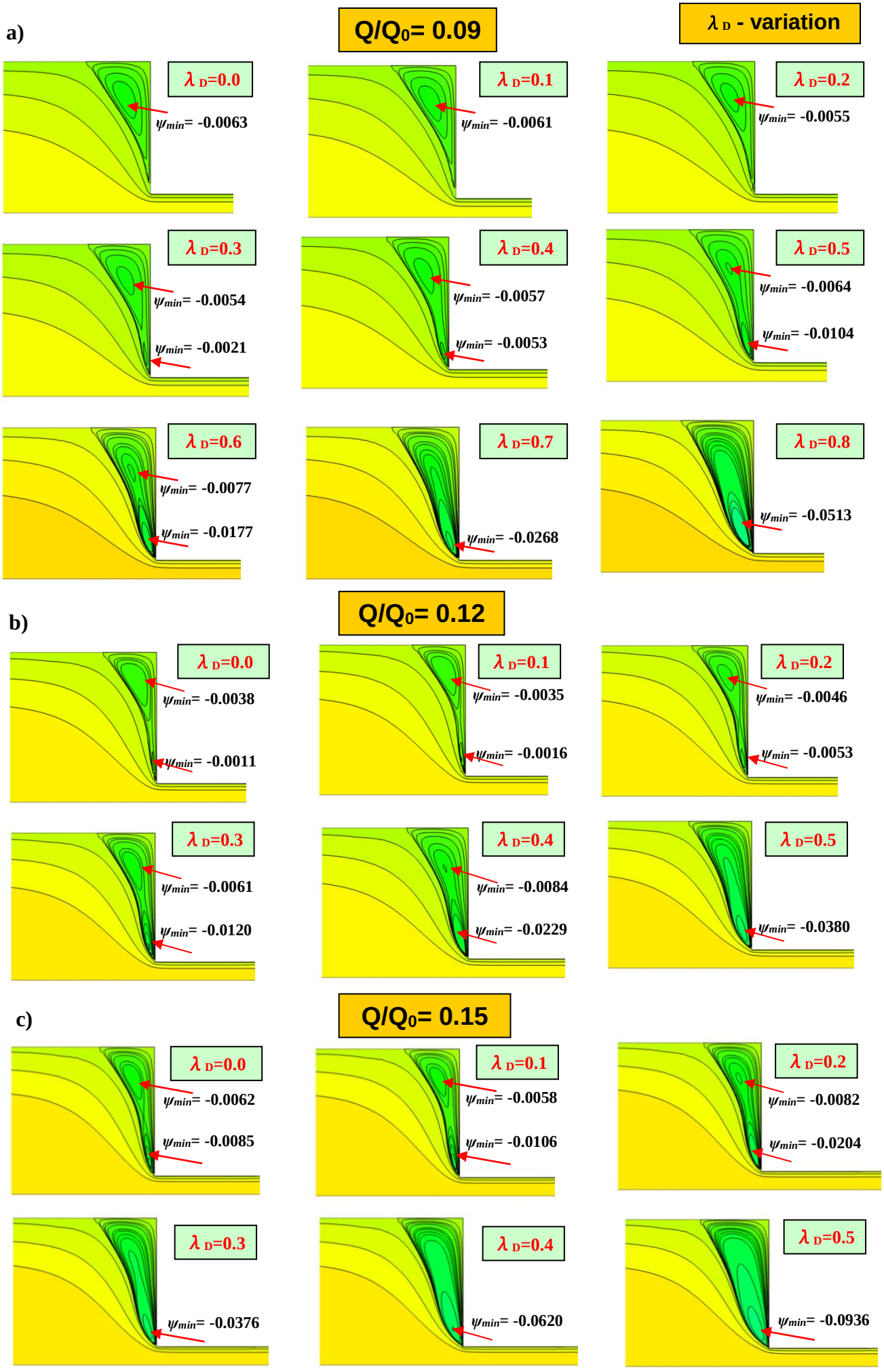

Figure 13. Streamlines, a) Q/Q_0=0.12, b) Q/Q_0=0.12, c) 0.15; *swIM*[β=0.9, L=5], various λ_D

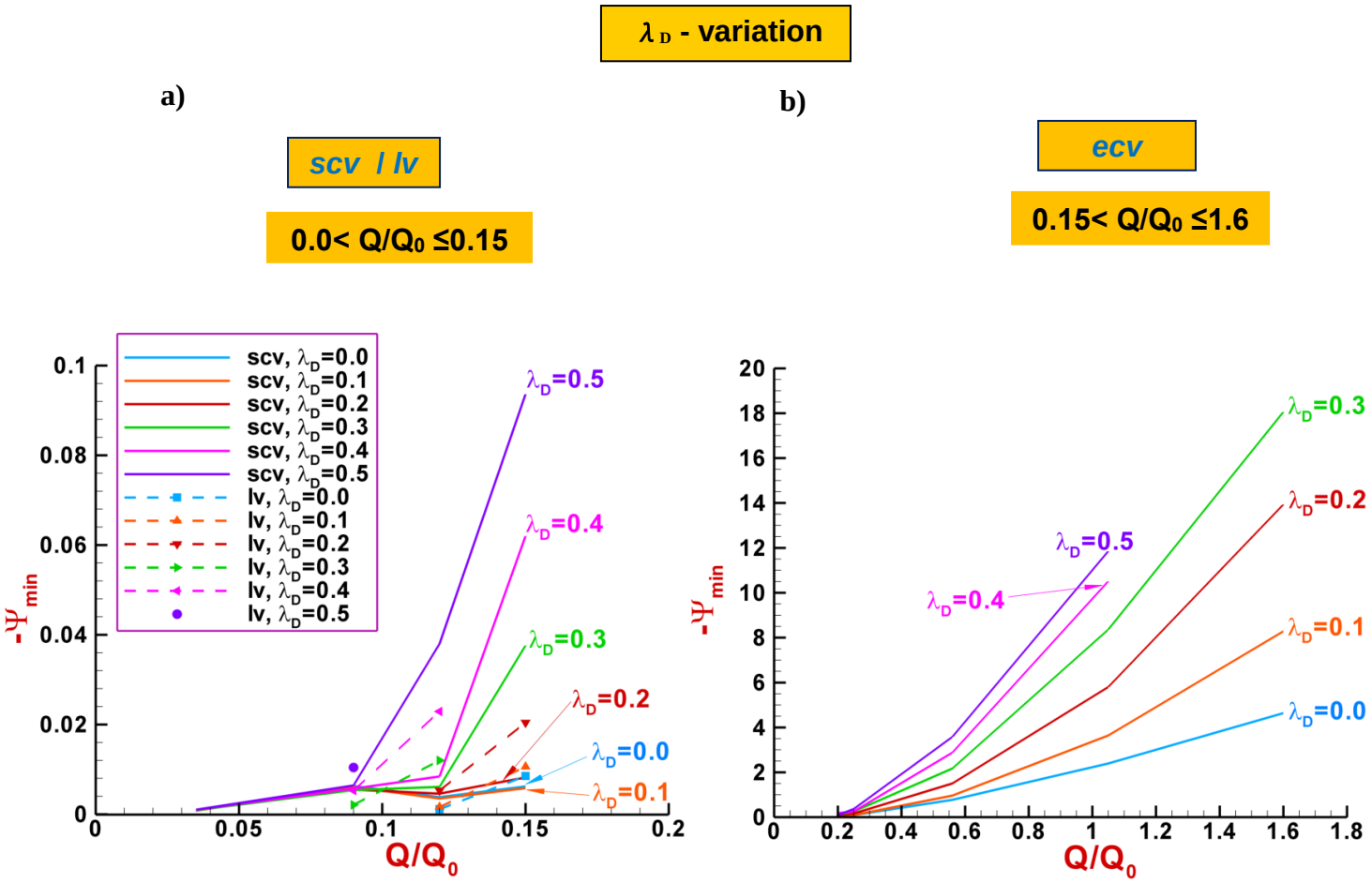

Figure 14. a) Salient, lip, and b) elastic-corner vortex intensity (ψ_{min});
swIM[β=0.9, L=5], 0<Q/Q_0≤1.6, various λ_D